Geometric & radiometric vignetting associated with a 72-facet, off-axis, polygon mirror for swept source optical coherence tomography (SS-OCT)

Michael Everson, Virgil-Florin Duma, and George Dobre

Citation: AIP Conference Proceedings **1796**, 040004 (2017); doi: 10.1063/1.4972382
View online: http://dx.doi.org/10.1063/1.4972382
View Table of Contents: http://aip.scitation.org/toc/apc/1796/1
Published by the American Institute of Physics

Geometric & Radiometric Vignetting Associated with a 72-Facet, Off-Axis, Polygon Mirror for Swept Source Optical Coherence Tomography (SS-OCT)

Michael Everson[1,a)], Virgil-Florin Duma[2,3,4] and George Dobre[1]

[1]*Applied Optics Group (AOG), School of Physical Sciences (SPS), University of Kent, Canterbury, CT2 7NH, UK*
[2]*3OM Optomechatronics Group, "Aurel Vlaicu" University of Arad, 77 Revolutiei Ave, Arad 310130, Romania.*
[3]*Doctoral School, Polytechnic University of Timisoara, 1 Mihai Viteazu Ave, Timisoara, 300222, Romania*
[4]*School of Physics, West University of Timisoara, 4 Vasile Parvan Ave, Timisoara, 300223, Romania*

[a)] Corresponding author: mje23@kent.ac.uk

Abstract. Optical Coherence Tomography (OCT) has a broad range of applications in 2D and volumetric imaging of micron scale structures typically used on inaccessible objects such as the retina of the eye. This report focuses on Swept Source OCT (SS-OCT), favoured for its faster scanning speeds and therefore faster data acquisition (highly favourable when imaging live patients). SS-OCT relies on the scanning of a narrow laser line at speeds typically in excess of 100 kHz. We have employed Zemax^{TM} ray tracing software to simulate one method of splitting the spectrum of a broadband, near-infrared source, into its component wavelengths by reflecting the spectrum from an off-axis, 72-facet polygon mirror at a frequency of 48 kHz. We specifically addressed the geometric and radiometric vignetting associated with the reflected spectrum off an individual mirrored facet and how this may impose limitations to the incident beam size and hence lead to a loss in the power available from the source. It was found that for certain configurations up to 44% of the light was lost at the edges of the spectrum due to both radiometric and geometric vignetting, which may result in an effective swept range of <50 nm from an initial bandwidth of 100 nm. Our simulations account for real refractive errors and losses in the beam caused by lens aberrations, and produce a model of the sampling function of wavelength against time.

INTRODUCTION

Optical Coherence Tomography (OCT) has firmly established its application as a practical imagining technique, capable of resolving micrometre scale details within small, three-dimensional volumes [3]. Its strength in providing useful information on this scale, without harmful invasion, on the structure and complexities of otherwise inaccessible materials has elevated its primary use as a medical diagnostics tool but still holds a variety of secondary uses as an investigative device that can be applied to a number of everyday objects and situations [1].

The continual evolution of OCT has produced a number of techniques that can either be: a) set up to perform one specific imaging or measurement task; or b) tailored to suit more general applications. This study focused on the technique known as Swept Source OCT (SS-OCT) [2], specifically applying to case b), and addresses the mechanical method by which a broad spectrum of light, with a spectral width $\Delta\lambda$ and centred at a wavelength λ_c, is filtered into narrow band windows of width $\delta\lambda$, which are separated from one another through the use of a Spectral Filter (SF) consisting of a dispersive element, a rotating Polygon Mirror (PM) and other optical components arranged in a Littman configuration [4,11,16].

Three key parameters determine the performance of SS-OCT, namely the axial depth resolution δz, the maximum axial imaging range Δz and the speed of operation (i.e. the frequency of the wavelength sweep). In this paper we are evaluating the effect of the SF optical design on the first two, which are given by:

TIM15-16 Physics Conference
AIP Conf. Proc. 1796, 040004-1–040004-9; doi: 10.1063/1.4972382
Published by AIP Publishing. 978-0-7354-1462-4/$30.00

$$\delta z = \frac{2\ln 2}{\pi} \cdot \frac{\lambda_c^2}{n\Delta\lambda} \tag{1}$$

$$\Delta z = \frac{\lambda_c^2}{2n\delta\lambda} \tag{2}$$

where n is the refractive index of the sample.

The advantage of a mechanical setup of the type discussed in this paper allows the ability to deploy the OCT method to perform laboratory imaging on a variety of samples without the inconvenience of replacing key components that would otherwise require major realignment [2]. Replacing the source for another bandwidth to image different materials only requires undoing a few fibre optic cables and the telescope geometry can be made to work at different wavelengths with minimal adjustment, which does not drastically interfere with the operation of the device.

Another advantage is the data acquisition speed, which is favourable for imaging tissue in live patients to reduce blurring artefacts. The PM in this experiment is capable of a maximum facet repetition rate of 65.935 kHz and, with a suitable buffering method to increase sweep density, can potentially achieve four times this value at speeds in excess of 260 kHz. With rigorous optimization it is expected that much higher speeds, >400 kHz, can be achieved [6, 8-15].

Due to the mechanical nature of this method, it was anticipated that the light reflecting off moving components may suffer from vignetting [7]; a consequence of the light rays striking an unwanted surface, in this case the adjacent mirrored facet of the PM (next to the active facet). The result will be that some light is lost even before it's used to scan the target and the loss would reduce the image resolution by limiting the effective bandwidth of the applied spectrum. It was therefore necessary to investigate this vignetting to assess quantitatively the detrimental impact it may impose on the system.

The use of a polygon mirror to produce a swept source places a fundamental constriction on the focal length, f_2, of the second lens in a telescopic system (Fig. 1). The minimum focal length is determined by the number of facets, n, on the polygon according to:

$$\frac{D}{f_{2\,min}} = 2\tan(\pi/n) \tag{3}$$

where D is the diameter of the second lens. This is because the image space numerical aperture of the lens needs to match the angular sweep of a polygon facet. The number of facets on the polygon gives an angular displacement per facet that cannot be exceeded by the incident/reflected spectrum's angular sweep or else the light returned by the polygon will not be captured entirely by the lens.

Our study was carried out exclusively using industry-standard Zemax™ Ray Tracing Software (Zemax, LLC) to simulate the power loss in the SF as a consequence of the vignetting. The software made it possible to account for many features of the set up including real refractive errors and losses in the beam caused by lens aberrations. The simulations that followed examined the geometric and radiometric vignetting of the light propagating through the SF by observing the beams geometric spot on the facets and the encircled energy reaching the RM respectively.

METHOD

The experimental apparatus consists of a fibre optic array acting as an interferometer with object & reference arms, detector and a swept source. The swept source is realised by taking the light output of a semiconductor optical amplifier (SOA), operating with a central wavelength λ_c= 1350 nm, and sending it to the SF (Fig. 1)

Within the SF, the collimated spectrum is first spatially separated (dispersed) through the use of a transmission grating. This introduces an angular divergence between the narrow bands. These bands are made to converge and overlap onto the PM where they are reflected onto a Retroreflector Mirror (RM). As the polygon rotates it tunes through the spectrum to sequentially reflect only one narrow bandwidth at any one time off the RM. The part of the spectrum filtered in this way is then circulated to the array, with each of the narrow bandwidths sent sequentially to the sample for scanning (i.e. spectral sweeping). A single spectral sweep occurs every time a new facet rotates into the path of the incident spectrum, providing 72 sweeps for every rotation of the PM due to the 72 facets present on the PM.

Once narrowband light is reflected back from the sample it is guided towards the interferometer output where it recombines with light that travelled through the reference arm. The interferometric output of this superposition is then sent to the detector for processing into an image.

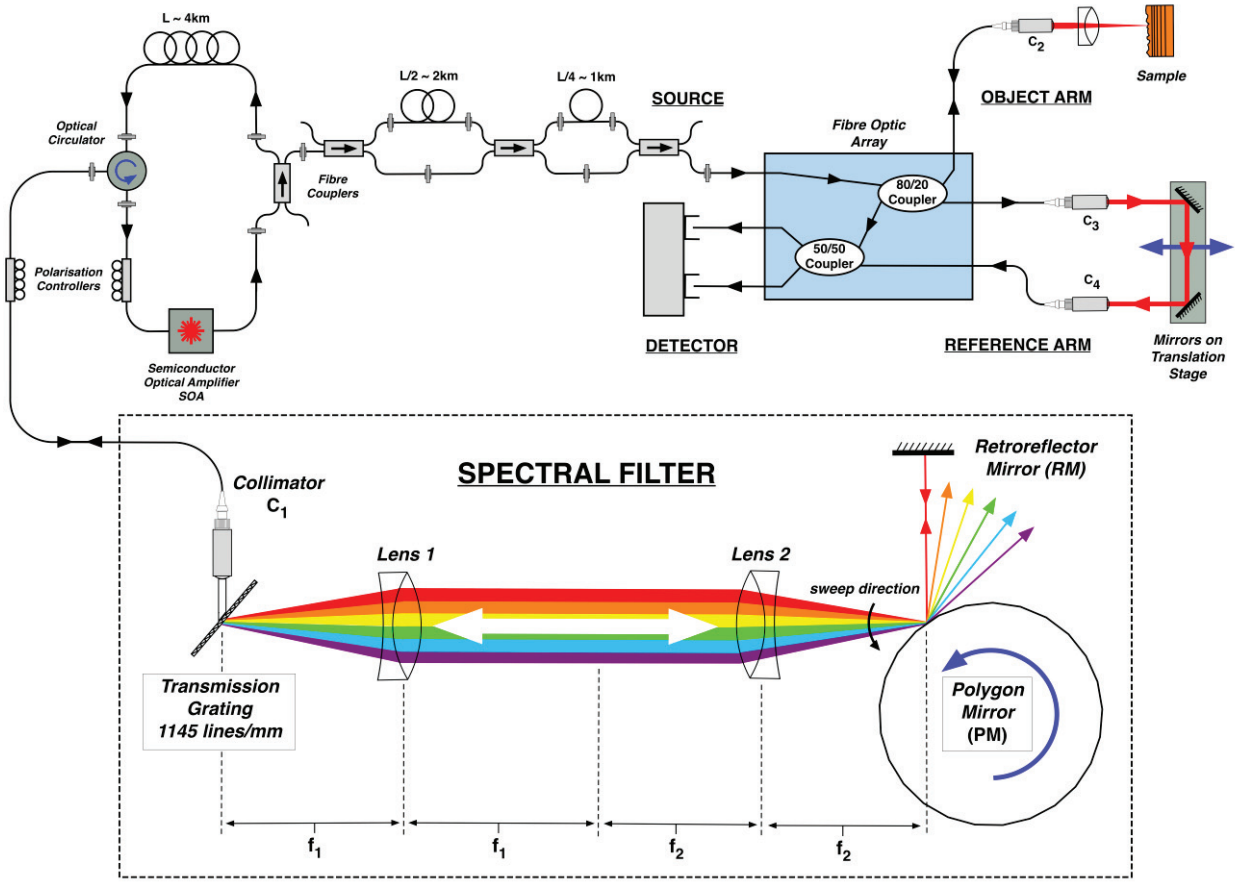

FIGURE 1. Experimental set up consisting of the fibre optic array interferometer with reference and sample arms, detector, optical circulator and spectral filter (SF)

The input spectrum traverses sequentially through the components as follows: transmission grating (Wasatch, 1145 lines/mm, 1310 nm, 47º operating angle), lens doublet 1 (Thorlabs achromatic AC254-75-C, f_1 = 75.0 mm), lens doublet 2 (Thorlabs achromatic AC254-100-C, f_2 = 100.0 mm), PM (SA34 Lincoln Laser, radius R = 31.75 mm, 72 facets, 5º/facet, facet dimensions = 2.77 mm width x 6.35 mm height) and RM. Exact specifications for these components were used in the simulation, including lens material, curvature and surface coatings.

SIMULATIONS, ASSUMPTIONS & RESULTS

Our ray tracing simulation consisted exclusively of the SF portion of the setup, originating from the 9 μm optical fibre placed before collimator C_1 (Thorlabs F280APC-C, f = 18.67 mm) in Figure 1, propagating left to right through the grating, telescope, PM and RM before returning and terminating at the same 9 μm optical fibre.

A 100 nm bandwidth centred at 1330 nm was assumed to enter at the input of C1. This bandwidth is sampled through nine individual wavelengths $\lambda_1 \ldots \lambda_9$ equidistantly spaced to represent the centres of narrowband windows throughout the spectrum.

Seven of nine central wavelengths were given a larger weight to provide a more accurate representation of the shape of the input spectrum produced by the SOA. The central five were given a relative weight of 1.5 while the remaining two used 1.25. (Table 1)

TABLE 1. Parameters for each of the nine wavelengths used in the simulation

Configuration No.	Wavelength λ_n (n = 1…9)	Weight	Polygon Angle (θ_n degrees) required for maximizing return into fibre
1	1280.00 nm	1.00	46.99
2	1292.50 nm	1.25	46.52
3	1305.00 nm	1.50	46.03
4	1317.50 nm	1.50	45.52
5	1330.00 nm	1.50	44.99
6	1342.50 nm	1.50	44.46
7	1355.00 nm	1.50	43.90
8	1367.50 nm	1.25	43.31
9	1380.00 nm	1.00	42.71

The rotation of the active PM facet, about the centre of the polygon, in steps of around 0.5º of angle, was found to result in the optimum propagation condition for each of the 9 configurations sequentially (i.e. maximum optical power is reinserted back into collimator C_1). The resulting angles θ_n are shown in Table 1. The arrangement is such that the optimum propagation angle for the central wavelength λ_5 = 1330 nm is set to θ_5 = 44.99º as shown in Fig. 3, (a) & (b).

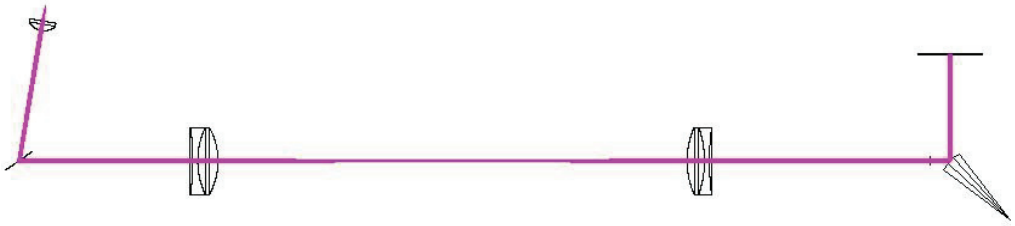

(a) Configuration 5, 1330 nm, 44.99°. Ideal scenario with no vignetting on the polygon.

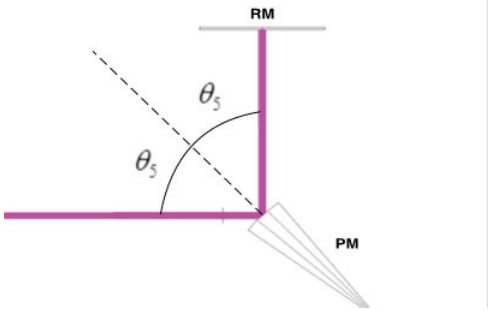

(b) Close-up of configuration 5. Incoming light travelling left to right reflects off the PM facet and onto the RM at normal incidence.

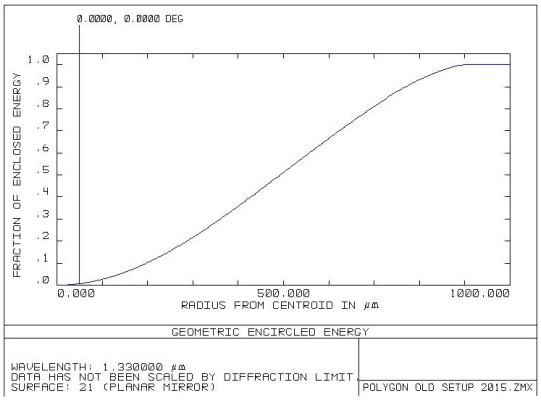

(c) Configuration 5, Geometric Encircled Energy Diagram. The slope is in agreement with the Gaussian intensity distribution of the source.

FIGURE 2. Simulation interface and analysis tools for assessing vignetting.

Figure 2 (c) depicts the fractional energy distribution from the centroid on the surface of the RM for configuration 5 at 1330 nm and a working angle of 44.99º. This is the chief ray of the spectrum and it shows the ideal no vignetting scenario whereby 100% of incident light reflects off the PM facet and onto the RM. Configuration 4 and 6 provide similar results also showing 100% transmission however as the configurations change through 4 to 1 and 7 to 9 it was shown that progressively less light is sent to the RM.

This study has resulted in two types of vignetting analysis:

- Geometric vignetting – expressed as area ratios on the facets
- Radiometric Vignetting – expressed as the fraction of energy measured at normal incidence on the RM

Geometric vignetting gives a measure of the fraction of the beams cross sectional area reaching the PM (taking into account the elliptical shape of the beam on the facets). Radiometric vignetting gives a measure of the fraction of total energy reaching the RM, as read out from the geometric encircled energy graphs.

Geometric Vignetting

The beam emitted from collimator C_1 has a diameter of 3.4 mm. However, we used a value of 3.0 mm in the simulation in order to be consistent with the fact that a narrower range of wavelengths is contained in each of the nine configurations.

Since the PM is positioned off-axis, meaning that the incident light beam does not strike each facet orthogonally but at an angle of approximately 45º, an elliptical spot will appear on the PM's facets. We ignored the 5º angle between adjacent facets in calculating the area of the ellipse corresponding to the beam area for each wavelength. The geometric coordinates of beam-facet intercepts are read off directly from Zemax and an approximate value for each wavelengths geometric vignetting is calculated.

The polygon angle θ_n is equal to the angle of incidence of the beam of wavelength λ_n on the facet. To calculate the proportion of the beam width that is not vignetted (i.e. it is returned successfully) we have used the ratio $\frac{y_2-y_1}{y_3-y_2}$ as a first order approximation of $\frac{\rho}{a}$ used in evaluating geometric vignetting according to the formula:

$$A_{segment} = \frac{ab}{4}\left[\cos^{-1}\left(1-\frac{2\rho}{a}\right) - \left(1-\frac{2\rho}{a}\right)\cdot\sqrt{\frac{4\rho}{a}-\frac{4\rho^2}{a^2}}\right] \tag{4}$$

where a is the major axis, b is the minor axis and ρ is the length along the major axis of the non-vignetted portion of the ellipse (Fig. 3).

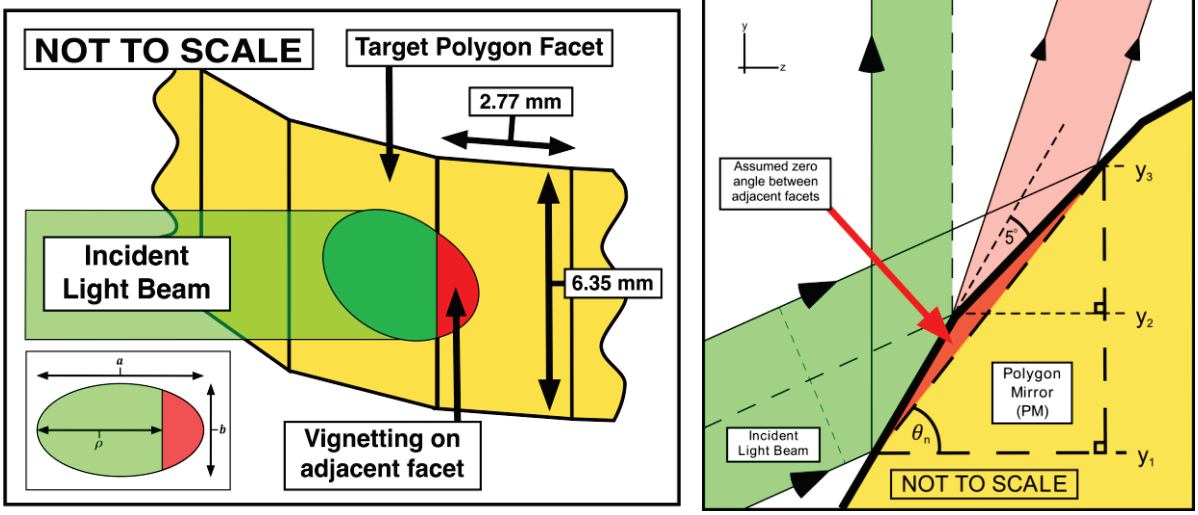

(a) This diagram illustrates the elliptical spot incident on the target facet and the vignetting associated with the adjacent facet.

(b) Values for the y-coordinates were taken directly from the simulations interface.

FIGURE 3. Facet geometry showing vignetting on adjacent polygon facet

It was found that nearly half of the incident light spectrum suffered from vignetting due to the geometry of the system. As much as 45.18% of the energy was lost at the edge of the spectrum relating to configuration 9 at 1380 nm.

The assumption we used (uniform power distribution in the beam) in order to calculate the portion of the elliptical spot falling on each of the facets has had the effect of providing a higher estimate for the fraction of vignetted light. This is consistent with the final results shown in the graph of Figure 6, which show slightly lower values than those obtained when examining the radiometric vignetting.

Radiometric Vignetting

The analysis discussed above, based on the ratio of ellipse areas, does not take into account the Gaussian intensity distribution of the beam, which favours rays located in the centre of the beam near the chief ray. In order to assess vignetting from the point of view of energy distribution, we used encircled energy diagram plots to provide information on the proportion of light in the non-vignetted part of the beam falling on the surface of the RM.

The encircled energy is measured radially from the center of mass of the total incident light energy. The majority of energy reaching the RM comes from the target facet meaning the center of mass is located closer to these rays, although not necessarily within them, and so the vignetted portion of the spectrum can be seen striking the RM at a larger radius. The example given in Figure 4 shows that the vignetted light does not hit the retroreflector mirror until approximately 6.5 mm away from the centroid (at R_3), and does so at an angle, which does not allow it to return to the polygon and back through the system.

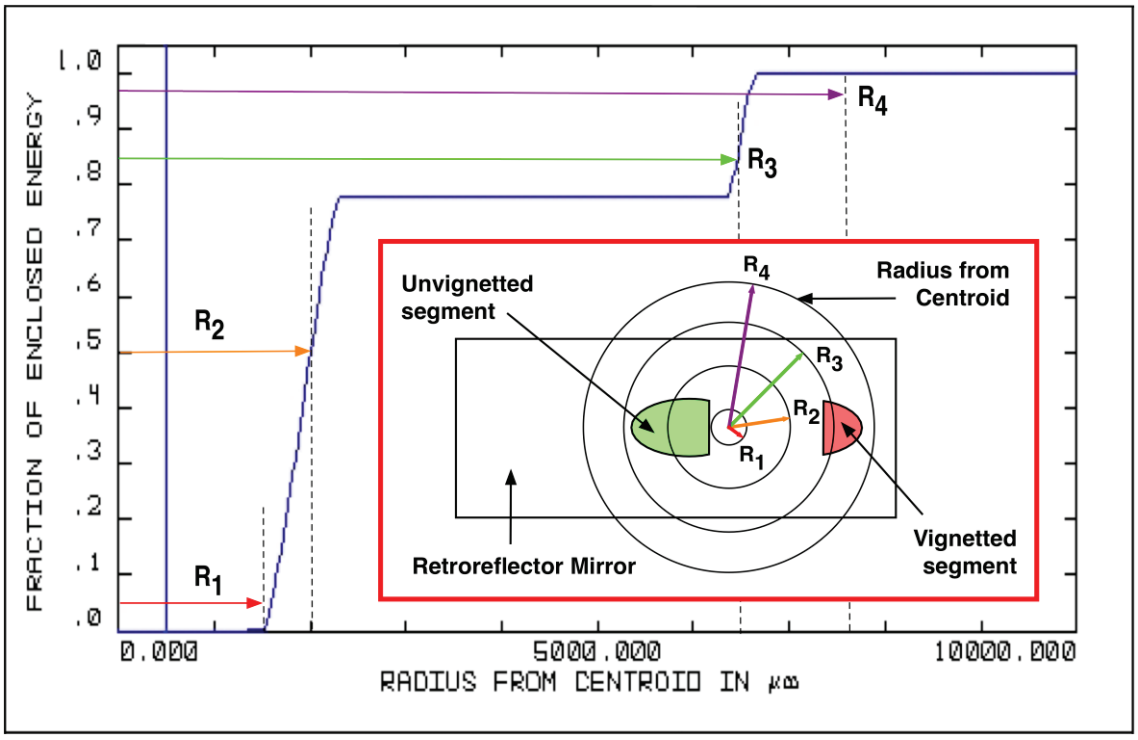

FIGURE 4. An example of a geometric encircled energy diagram plus an insert depicting the surface of the RM to provide a complete understanding of its interpretation. The total incident light energy on the RM has been separated radially at approximately 80%.

The remaining unvignetted light could be subsequently assumed to propagate successfully back through the telescopic arrangement, following the same trajectory as on the outward trip, and be recaptured in collimator C_1 however the encircled energy is computed as a function of the energy propagating through the previous surface, which is always taken to be 100%, so it is only possible to assess the lost light energy between two surfaces, i.e. between the light reflected off the PM (100%) and the light striking the RM at different radii due to the vignetting (unvignetted ~80%, vignetted ~20%).

This analysis also found that the central portion of the spectrum is reflected back in its entirety, while light at the edges undergoes vignetting. Figure 5 displays the images showing facet reflection (a) & (c) and their geometric encircled energy diagrams (b) & (d) resulting from configurations 1 and 9 at the extreme edges of the spectrum, whereby the light has been vignetted by the adjacent facets.

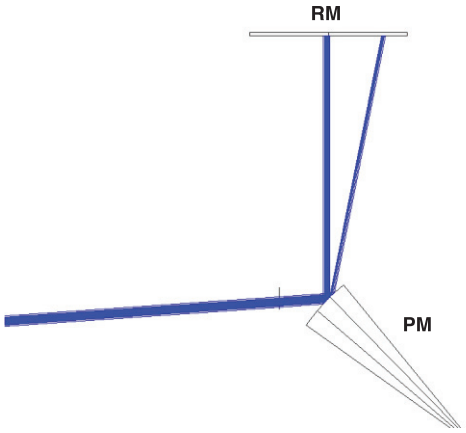

(a) Configuration 1, 1280 nm, 46.99º

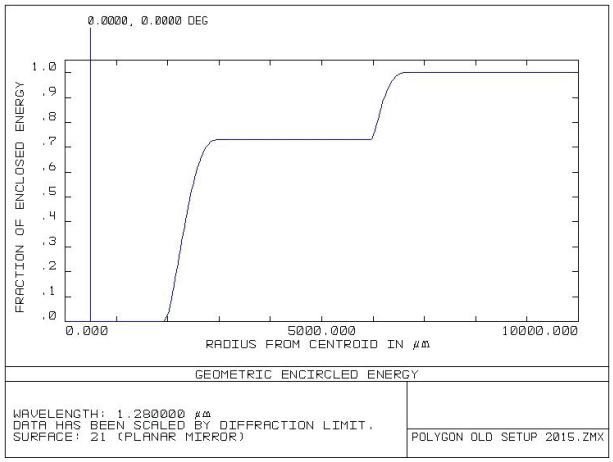

(b) Configuration 1, Geometric Encircled Energy Diagram

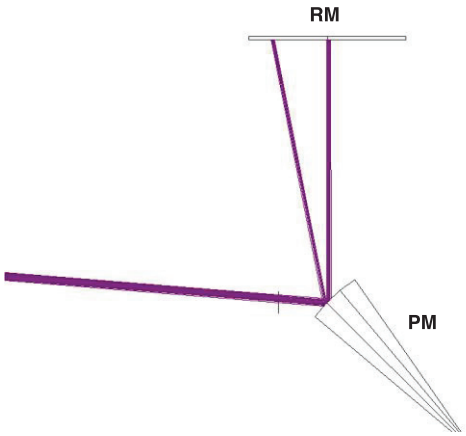

(c) Configuration 9, 1380 nm, 42.71º

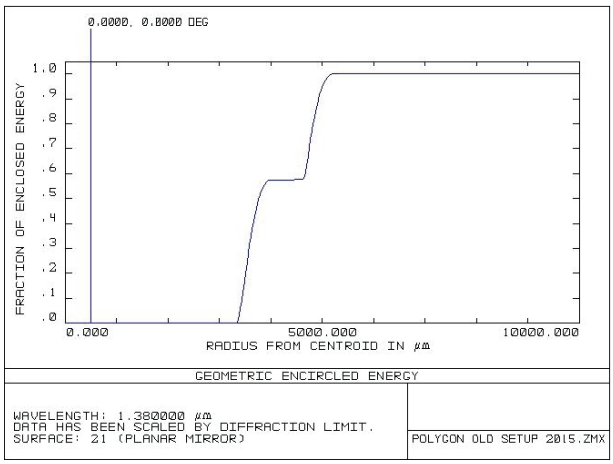

(d) Configuration 9, Geometric Encircled Energy Diagram

FIGURE 5. Geometric Encircled Energy diagrams for Configuration 1 and 9, used to determine the radiometric fraction of light propagating to the RM

In the case of Configuration 1, we obtain a total loss in radiation energy of >26% at the shorter wavelength limit of the spectrum, (bottom of spectrum in Fig. 1), and a loss of >43% for configuration 9 at the longer wavelength limit of the spectrum. The difference of 17% is due to the way the light has been vignetted in either configuration. Configuration 1 sees the light vignetted by the adjacent facet above the target facet while configuration 9 is vignetted by the facet below. The radial separation between the vignetted and un-vignetted light decreases as the distribution of energy becomes equal in both beams. Similar graphs are found for configurations 2 & 3 and 7 & 8, displaying an increase and decrease in radial separation respectively.

Figure 6 provides the comparison between radiometric and geometric vignetting. From the graph it is noticeable how the initial bandwidth of 100 nm has been clipped on either side of the incident spectrum to leave an effective bandwidth of only approximately 50 nm, with its edges still suffering from a fractional loss, meaning that roughly 40% of the initial bandwidth has suffered significant detrimental effects from facet vignetting. The Gaussian beam profile clearly has the effect of mitigating somewhat the effects of vignetting on adjacent facets in the radiometric vignetting case, while the geometric vignetting calculation assumed a uniform distribution.

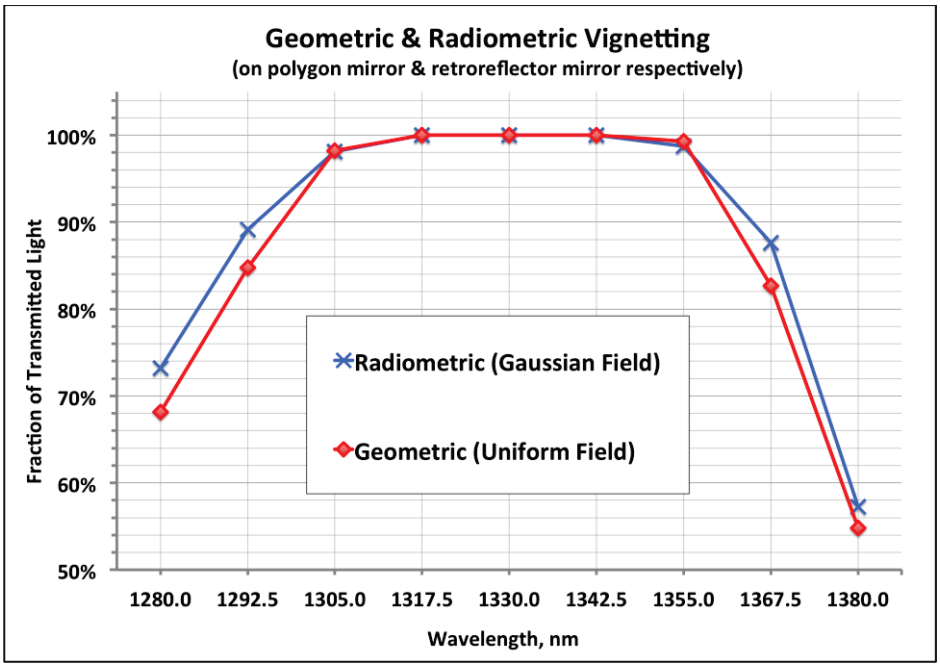

FIGURE 6. Variation of the fraction of light that is vignetted by the polygon mirrors facets as a function of wavelength

CONCLUSIONS

The reduced bandwidth results in a loss of optical power and a decrease in the image resolution as shown by equations 1 and 2, underlining the importance of this study in understanding how design considerations can affect the overall performance of the system.

In this study the vignetting is caused as a result of using the 72-facet polygon. A smaller number of facets with the same radius would result in larger facet areas and therefore would reduce or even remove the effect of vignetting altogether. However, this would have a detrimental effect on the speed of the tuning as the frequency is directly proportional to the number of facets. Therefore, a larger radius on the polygon should be employed but this has an impact on its maximum speed due to the manufacturing precession required, which would increase the cost of its production, it's fundamental limit being governed by the physics of the materials used and the assembly process.

Assessing the balance between polygon size and speed of rotation will be crucial if vignetting is to be removed from any polygon based swept source spectral filter. Since the ratio of the beam widths before and after the telescope is the same as the ratio of the focal lengths of lens 1 and lens 2, the constraints imposed by our vignetting analysis on the beam width at the telescope output may be satisfied through a different choice of telescope lenses and their respective diameters and focal lengths, while complying to the minimum value of f_2 required by the polygon (Eq. 3).

ACKNOWLEDGMENTS

Michael Everson acknowledges the support of the UK Engineering and Physical Sciences Research Council.

REFERENCES

[1] H. Liang, M. G. Cid, R. Cucu, G. Dobre, B. Kudimov, J. Pedro, D. Saunders, J. Cupitt and A. Podoleanu, *Proceedings of SPIE*, **5857**, Optical Methods for Arts and Archaeology, (2005).
[2] B. Bräuer, N. Lippok, S. G. Murdoch, and F. Vanholsbeeck, *Journal of Optics*, **17(12)**, 125301 (2015).
[3] M. A. Choma, M.V. Sarunic, C. Yang and J. A Izatt, *Optics express* **11(18)**, 2183-2189 (2003).
[4] M.G. Littman and H. J. Metcalf, *Applied optics* **17(14)**, 2224-2227 (1978).
[5] K. Liu and M.G. Littman, *Optics Letters* **6(3)**, 117-118 (1981).

[6] W. Y. Oh, B. J. Vakoc, M. Shishkov, G. J. Tearney and B. E. Bouma, *Optics letters* **35(17)**, 2919-2921 (2010).
[7] V. F. Duma, *Applied optics* **48(32)**, 6355-6364 (2009).
[8] S. H. Yun, C. Boudoux, G. J. Tearney and B. E. Bouma, *Optics letters* **28(20)**, 1981-1983 (2003).
[9] Y. Mao, C. Flueraru, S. Sherif and S. Chang, *Optics Communications* **282(1)**, 88-92 (2009).
[10] W. Y. Oh, S. H. Yun, G. J. Tearney and B. E. Bouma, *Optics letters* **30(23)**, 3159-3161 (2005).
[11] M. K. Leung, A. Mariampillai, B. A. Standish, K. K. Lee, N. R. Munce, I. A. Vitkin and V. X. Yang, *Optics letters* **34(18)**, 2814-2816 (2009).
[12] Y. S. Kwon, M. O. Ko, M. S. Jung, I. G. Park, N. Kim, S. P. Han, H. C. Ryu, K. H. Park and M. Y. Jeon, *Sensors* **13(8)**, 9669-9678 (2013).
[13] Y. Mao, S. Chang, E. Murdock and C. Flueraru, *Optics letters* **36(11)**, 1990-1992 (2011).
[14] S. W. Lee, H. W. Song, M. Y. Jung and S. H. Kim, *Optics express* **19(22)**, 21227-21237 (2011).
[15] S. M. Nezam, *Optics letters* **33(15)**, pp.1741-1743 (2008).
[16] C. Palmer, *Diffraction Grating Handbook – 5th Edition*, edited by E. Loewen (Thermo RGL, Rochester, New York, 2002), p. 19.